Composition change of stainless steel during microjoining with short laser pulse

X. He and T. DebRoy[a)]
Department of Materials Science and Engineering, The Pennsylvania State University, Pennsylvania 16802-5005

P. W. Fuerschbach
Joining and Coating Department, Sandia National Laboratories, Albuquerque, New Mexico 87185-0889

(Received 1 June 2004; accepted 29 June 2004)

Weld metal composition change in 200 μm deep, 304 stainless steel microjoints fabricated using millisecond long Nd-YAG laser pulses was investigated experimentally and theoretically. The variables studied were pulse duration and power density. After welding, concentrations of iron, manganese, chromium, and nickel were determined at various locations of the microjoint using the electron microprobe analysis. The temperature field was simulated as a function of time from a well-tested three-dimensional transient heat transfer and fluid flow model. Using the computed temperature fields, vaporization rates of various alloying elements resulting from both concentration and pressure driven transport of vapors and the resultant composition change of the alloy were calculated. The calculations showed that the vaporization took place mainly from a small region near the center of the beam-workpiece interaction zone, where the temperatures were very high. Furthermore, the alloying element vaporization was most pronounced toward the end of the pulse. After the laser spot welding, the concentrations of manganese and chromium in the weld pool decreased, whereas the concentrations of iron and nickel increased. The composition changes predicted by the model were in fair agreement with the corresponding experimental results for various conditions of microjoining with short duration pulses. © *2004 American Institute of Physics*. [DOI: 10.1063/1.1785868]

I. INTRODUCTION

The joining of very small metallic components is often accomplished with short laser pulses of only a few milliseconds duration. The laser microjoining is characterized by its small length scale, fairly short duration, highly transient nature, and very high heating and cooling rates.[1] Because of the high power density used, the weld metal is rapidly heated to very high temperatures, and as a consequence, significant vaporization of volatile alloying elements often takes place from the weld pool surface.[2–11] Previous work on linear laser welds has shown that the composition of many important industrial alloys can change significantly owing to selective vaporization of alloying elements. The composition change, in turn, can lead to significant changes in the microstructure and degradation of the mechanical and corrosion properties of the welds.

The vaporization of the alloying elements during microjoining is different from that during linear welding in several ways. First, the evaporation rate is strongly time dependent i.e., the rate is negligible at the initiation of the pulse and gradually increases owing to the increase in temperature. Second, because of the short duration of the laser pulse, the experimental determination of temperature and velocity fields is difficult and remains both an important goal and a major challenge in the field. Third, although both the surface area and the volume of the weld pool are small, they change significantly with time. As a result of these difficulties, very little information is available in the literature about measurement of important variables, such as the temperature field, during microjoining.

In a recent paper in this journal,[12] an experimental technique was proposed to determine an approximate value of the peak temperature in the weld pool from the vapor composition during irradiation by a pulsed laser beam. Composition of the metal vapor from the weld pool was determined by condensing a portion of the vapor on the inner surface of a both end open quartz tube, which was mounted perpendicular to the sample surface and coaxial with the laser beam. The vapor composition was used to determine an effective temperature of the weld pool for various welding conditions. This technique is shown to be a useful method to determine the approximate values of peak temperature during laser sport welding. However, peak temperature is only one of the factors in the understanding of alloying element vaporization during laser welding. Once the liquid pool forms, a strong spatial gradient of temperature exists on its surface. The resulting gradient of surface tension is the main driving force for the recirculating flow of molten metal in the weld pool. In addition, the buoyancy force resulting from the spatial variation of density also contributes to the motion of the weld pool although to a much lesser extent than the surface tension gradient.[1,13–15] Because of the strong recirculating flow, the weld pool can be reasonably assumed to be well mixed and compositionally homogeneous. For a weld pool of a known composition, the vaporization rates of various al-

[a)]Electronic mail: debroy@psu.edu

TABLE I. Composition of 304 stainless steel.

Alloying element	Mn	Cr	Ni	Si	C	P	S	Fe
wt %	1	18.1	8.6	0.69	0.046	0.012	0.003	balance

loying elements are strongly affected by the surface temperatures. In order to minimize the mass loss during high power laser welding, it is necessary to quantitatively understand the role of various factors, such as the temperature distribution on the surface, the weld metal chemical composition, and the weld surface area that affect vaporization of alloying elements during laser assisted microjoining.

Numerical models have been used to understand the heat transfer and fluid flow during both the linear and spot welding. These models have been widely utilized to quantitatively understand the thermal cycles and fusion zone geometry.[16–24] Results from the heat transfer and fluid flow study have also been used to study the weld phase composition in the linear welds,[25–27] inclusion structures,[28–30] grain structure,[31–33] and for the prevention of porosity in the welds.[34] However, most of these studies were focused on the linear steady-state welds and not on the very short duration laser assisted microjoining. Although a limited number of investigations of spot welds have been undertaken in the past, time scales studied were much longer than the typical few milliseconds involved in the laser spot welds. A detailed experimental and theoretical study of the alloy composition change during laser assisted microjoining has not been undertaken.

In this paper, recent experimental and modeling results of composition change in stainless steel during laser assisted microjoining are examined. Concentrations of iron, manganese, chromium, and nickel were determined at various locations of the microjoint using the electron microprobe analysis. A transient, three-dimensional numerical heat transfer and fluid flow model based on the solution of the equations of conservation of mass, momentum, and energy was used to calculate the temperature and velocity fields in the weld pool as a function of time. Using the computed temperature profiles as a function of time, the vaporization rates and the weld metal compositional changes are computed. Model predictions of compositional changes are compared with the corresponding experimentally measured values.

II. EXPERIMENTAL PROCEDURE

Specimens of 304 stainless steel were irradiated with Nd-YAG (Neodymium-yttrium aluminum garnet) laser pulses of different power density and duration at Sandia National Laboratories. The alloy composition is given in Table I. Individual spot welds from a pulsed laser beam were made on $3\times10\times17$ mm EDM (Electrical Discharge Machining) wire cut samples. A Raytheon SS 525 pulsed Nd:YAG laser was used for the experiments. The welding conditions were varied by changing the input energy, pulse duration, and beam radius. The input energies of 2.1, 3.2, and 5.9 J and pulse durations of 3.0 and 4.0 ms were used, respectively. For each combination of input energy and pulse duration, the various laser beam radius were obtained by defocusing the laser beam to different extents. Supplementary argon shielding was provided to reduce the oxide formation and for the protection of the lens during welding. Up to 15 individual spot welds were made on each of the samples. After welding, the concentrations of iron, manganese, chromium and nickel along the radial direction of the weld pool were traced by the electron microprobe. Because the other alloying elements constitute less than 1 wt %, they were not recorded.

TABLE II. Data used for calculations.

Property/Parameter	Value[a]
Density of liquid metal (kg/m^3)	7.2×10^3
Absorption coefficient	0.27
Effective viscosity (kg/m s)	0.1
Solidus temperature (K)	1697
Liquidus temperature (K)	1727
Enthalpy of solid at melting point (J/kg)	1.20×10^6
Enthalpy of liquid at melting point (J/kg)	1.26×10^6
Specific heat of solid (J/kg K)	711.8
Specific heat of liquid (J/kg K)	837.4
Thermal conductivity of solid (J/m s K)	19.26
Effective thermal conductivity of liquid (J/m s K)	209.3
Temperature coefficient of surface tension (N/m K)	-0.43×10^{-3}
Coefficient of thermal expansion	1.96×10^{-5}
Diameter of nozzle (m)	0.006

[a]See References 38–42.

III. MATHEMATICAL MODELING

A. Transient temperature profiles

A numerical model to simulate heat transfer and fluid flow in the weld pool was used to calculate the temperature and velocity fields in the weld pool during both heat and cooling. This transient model has been extensively validated[1,12,24,27,29,32,35–37] and has been used to calculate the weld pool geometry, temperature, and velocity fields during welding of pure iron,[24,37] steel,[1,8,11,12,29,35,36] aluminum alloy,[9] and titanium alloy[32] under different welding conditions. Calculations were made for both the moving and the stationary heat sources and for the laser beam, arc, and hybrid welding. The assumptions, the model framework, and the solution procedure have been described in details in recent papers[1,35] and are not repeated here. The computed temperature fields as a function of time are then used to calculate the vaporization rates and the composition change of the alloying elements. The data used for the calculations[38–42] are presented in Table II.

B. Vaporization due to concentration gradient

On the weld pool surface, the concentrations of the alloying elements in the vapor are higher than those in the bulk shielding gas. The diffusive vaporization flux of the element i, J_{ci}, can be defined as

$$J_{ci} = K_{gi}\left(M_i\frac{a_i p_i^0}{RT_l} - C_i^s\right), \tag{1}$$

where M_i is the molecular weight of the element i a_i, is the activity of the element i in the liquid metal, P_i^0 is the equi-

librium vapor pressure of the element i over its pure liquid, R is the gas constant, T_l is the temperature on the weld pool surface and is obtained from the transient heat transfer and fluid flow model, C_i^s is the concentration of the element i in the shielding gas, and K_{gi} is the mass transfer coefficient of the element i between the weld pool surface and the shielding gas. Its value is calculated from the graphical results of Schlunder and Gniclinski [43] for a jet impinging on a flat surface and can be expressed by

$$K_{gi} = \frac{2Sc^{0.42}Re^{0.5}D_i}{d}\left(1+\frac{Re^{0.55}}{200}\right)^{0.5}\left[0.483 - 0.108\frac{r}{d} + 7.71\times 10^{-3}\left(\frac{r}{d}\right)^2\right], \quad (2)$$

where Sc is the Schmidt number, Re is the Reynolds number at the nozzle exit, D_i is the average diffusivity of the element i in the shielding gas, d is the diameter of the shielding gas supply nozzle, and r is the radial distance on the weld pool surface.

C. Vaporization due to pressure gradient

During laser welding, the peak temperature reached on the weld pool surface often exceeds the boiling point of the alloy. As a result, the vapor pressure on the weld pool surface can be higher than the ambient pressure, and the excess pressure provides a driving force for the vapor to move away from the surface. Therefore, the convective flux of the vaporized elements, driven by the excess pressure, is an important contributor to the overall vaporization flux.

On the weld pool surface, the molecules cannot travel in the negative direction, and as a consequence, the velocity distribution is half-Maxwellian. Close to the weld pool, there exits a space of several mean-free-paths length, known as the Knudsen layer, at the outer edge of which the velocity distribution just reaches the equilibrium distribution. A portion of the vaporized material condenses on the liquid surface. The rate of the condensation was taken into account in the model.

The temperature T_v, the density ρ_v, the pressure P_v, and the mean velocity u of the vapor at the edge of the Knudsen layer can be related to the temperature T_l, density ρ_l, and pressure P_l of the vapor on the liquid surface by treating the Knudsen layer as a gasdynamic discontinuity. Anisimov and Rakhmatulina[44] and Knight[45] derived expressions for the vapor temperature, density, velocity, and the extent of the condensation across the Knudsen layer by solving the equations of conservation of mass, momentum, and translational kinetic energy. The derived jump conditions across the Knudsen layer are given by

$$\frac{T_v}{T_l} = \left[\sqrt{1+\pi\left(\frac{\gamma_v-1}{\gamma_v+1}\frac{m}{2}\right)^2} - \sqrt{\pi}\frac{\gamma_v-1}{\gamma_v+1}\frac{m}{2}\right]^2, \quad (3)$$

$$\frac{\rho_v}{\rho_l} = \sqrt{\frac{T_l}{T_v}}\left[\left(m^2+\frac{1}{2}\right)e^{m^2} - erfc(m) - \frac{m}{\sqrt{\pi}}\right] + \frac{1}{2}\frac{T_l}{T_v}\left[1-\sqrt{\pi}me^{m^2} - erfc(m)\right], \quad (4)$$

$$\beta = \left[(2m^2+1) - m\sqrt{\pi\frac{T_l}{T_v}}\right]e^{m^2}\frac{\rho_l}{\rho_v}\sqrt{\frac{T_l}{T_v}}, \quad (5)$$

where $m = u/\sqrt{2R_vT_v}$, $R_v = R/M_v$, R is the gas constant, M_v is the average molecular weight of the vapor, γ_v is the ratio of specific heat of the vapor, which is treated as a monatomic gas, $erfc$ is the complimentary error function, and β is the condensation factor. In order to solve these equations, an additional equation is obtained by applying the Rankine-Hugoniot relation[46] to relate the pressure at the edge of the Knudsen layer to the ambient conditions

$$\frac{P_1}{P_g}\frac{P_2}{P_l} = 1 + \gamma_g M\Gamma\left[\frac{\gamma_g+1}{4}M\Gamma + \sqrt{1+\left(\frac{\gamma_g+1}{4}M\Gamma\right)^2}\right], \quad (6)$$

where P_g and P_2 are the pressures in front of and behind the wavefront, respectively, $P_2 = P_v$, γ_g is the ratio of the specific heats for the shielding gas, $\Gamma = \sqrt{\gamma_v R_v T_v}/\sqrt{\gamma_g R_g T_g}$, and M is the Mach number. The Mach number M and the density ρ_v, obtained by solving the previous equations, can be used to calculate the vaporization flux due to the pressure gradient on the weld pool surface corresponding to a local surface temperature T_1

$$J_p = \rho_v MS, \quad (7)$$

where S is the speed of sound in the vapor at temperature T_v. Since the rate of the vaporization of an alloying element is proportional to its partial pressure over the weld pool, the vaporization flux of the element i, J_{pi}, due to pressure gradient can be given by

$$J_{pi} = a_i\frac{P_i^0}{P_l}\frac{M_i}{M_v}J_p. \quad (8)$$

A more detailed procedure for the calculation of the total vaporization flux due to the pressure gradient is available elsewhere.[8]

D. Vaporization rate and composition change due to vaporization

The total vaporization flux for the element i is the sum of the diffusion driven flux, J_{ci}, and pressure driven vapor flux, J_{pi}, and can be given by

$$J_i = J_{ci} + J_{pi}. \quad (9)$$

The vaporization rate is obtained by integrating the vapor flux over the entire weld pool surface. The vaporization rate of the element i is given by

$$G_i = \int_s\int J_i dxdy, \quad (10)$$

where s indicates the weld pool surface; the weight loss of the element i can be calculated by

$$\Delta m_i = \sum_t \int \int_s J_i \Delta t dx dy, \tag{11}$$

where Δt is the time step. The initial weight percent of the element i is chosen to be that of the base metal, indicated by W_{bi}. The weight percent of the element i, W_i in the weld pool can be calculated by

$$W_i = \frac{V\rho W_{bi} - \Delta m_i}{V\rho - \Sigma_{i=1}^{n} \Delta m_i} \times 100\,\%\,, \tag{12}$$

where V is the volume of the weld pool, ρ is the density of the liquid metal, and the variable n indicates the number of elements in the vapor. The final composition in the weld pool is calculated by an interactive scheme. After each iteration, the composition of the alloying elements in the weld pool is updated. Using the new values of composition of the alloying elements, all the calculations are repeated until the calculated composition in the weld pool converges. The concentration change of the element i is the difference of the final weight percent in the weld pool and the weight percent of the element i in the base metal,

$$\Delta W_i = W_i - W_{bi}. \tag{13}$$

IV. RESULTS AND DISCUSSION

When very high power density energy sources, such as laser and electron beams, are irradiated on the surface of a solid alloy target, the substrate is heated by the absorbed energy rapidly, the alloy melts, and a liquid weld pool forms. At this stage, the concentrations of the metal vapors are higher near the weld pool surface than in the bulk shielding gas. The vapor flux is driven mainly by the diffusion in the gas phase outside the liquid pool. As the temperature of the liquid pool continues to increase and reaches its boiling point, the pressures on the weld pool surface are higher than the ambient pressure, and the excess pressure provides a driving force for the vapor to move away from the surface. The temperature distribution at the weld pool surface determines whether a concentration or a pressure gradient is the main driving force for the vaporization.

A. Computed temperature fields and weld pool geometry

Figures 1(a)–1(c) show the computed temperature and velocity fields at 1, 2, and 3 ms, respectively. The liquid-metal motion is driven mainly by the Marangoni force and to a much lower extent by the buoyancy force.[1] Because the surface tension decreases with the increase in temperature, the Marangoni force drives the liquid metal from the center to the periphery at the top surface of the weld pool. As a result, the weld pool becomes wide and shallow. During the heating by the laser beam, the weld pool grows in size and the temperatures and velocity of the liquid metal increase with time. The maximum velocity of the liquid along the x direction in the weld pool is 0.91 m/s. Using this value of velocity, the Peclet number for the heat transfer, Pe, is found to be 9.50. Because this value is much greater than 1, heat is transported mainly by convection within the weld pool.

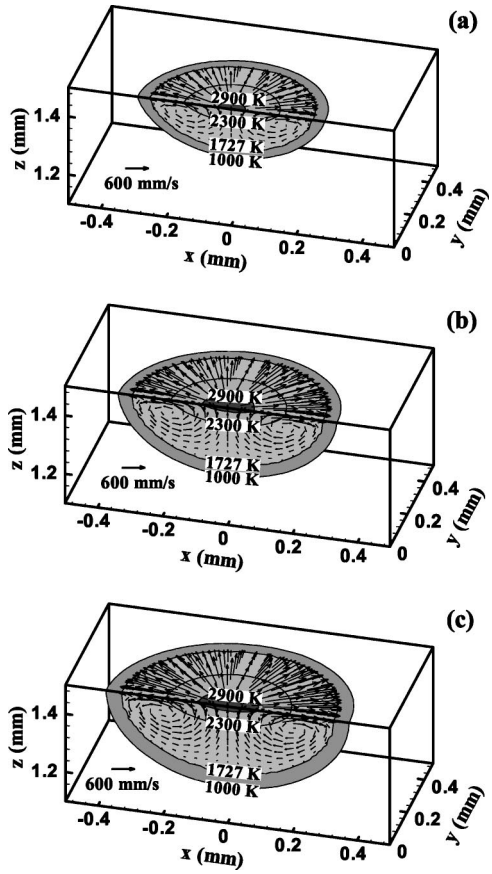

FIG. 1. Computed temperature and velocity fields at different times: (a) $t=1$ ms, (b) $t=2$ ms, and (c) $t=3$ ms. Laser power: 1067 W, pulse duration: 3 ms, and spot radius: 0.26 mm.

Figure 2 shows the computed peak temperature and the volume of the weld pool as a function of time. During the initial period of about 1 ms, the temperature increases rapidly and then grows slowly until the end of pulse duration. As a consequence, most of the vaporization occurs during the last 2 ms. Unlike the temperature, the volume of the weld pool increases almost linearly with time for the entire 3 ms period. This result clearly shows that a steady state is not reached for the entire duration of the pulse. After the laser is switched off, the temperature decreases rapidly and consequently, the weld pool shrinks with time. It takes about 1.2 ms after the power is switched off for the weld pool to solidify completely. The computed results show that the peak temperature can exceed the boiling point of the alloy. Under this condition, the equilibrium vapor pressure on the liquid surface is higher than one atmosphere, and the vaporization is mainly driven by the pressure gradient.

The effect of power density on the peak temperature and weld pool volume is shown in Fig. 3. The peak temperature in this figure is computed at the end of the pulse. It is interesting to note that the weld pool volume at the end of 3 ms does not increase significantly above 2000 W/mm^2, whereas the peak temperature increases continuously even beyond this power density. Clearly, the weld pool volume is limited by the rate of heat transfer in the solid region above

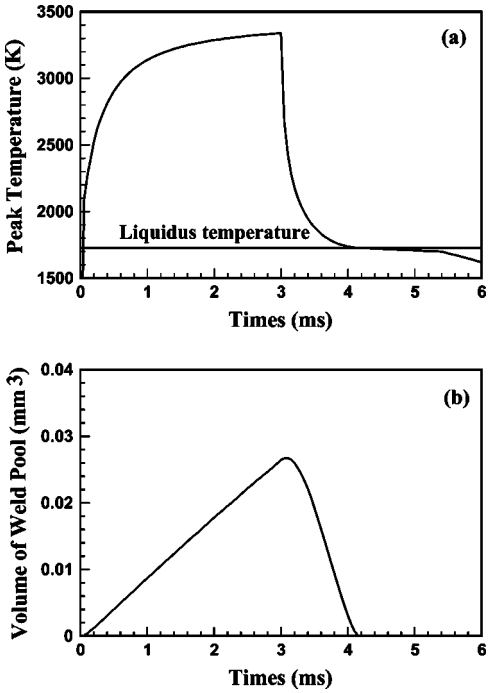

FIG. 2. (a) Computed peak temperature and (b) volume of the weld pool as a function of time. Laser power: 1067 W, pulse duration: 3 ms, and beam radius: 0.26 mm.

2000 W/mm^2, whereas the deposition of higher power density locally does increase the peak temperature.

B. Vaporization rate

Because the weld pool surface temperatures reach fairly high values, pronounced vaporization of the alloying elements takes place during laser spot welding. The Langmuir equation is often used to calculate the vaporization flux because of its simplicity[47]

$$J_i = \frac{P_i}{\sqrt{2\pi M_i RT}}, \tag{14}$$

where P_i is the vapor pressure over the alloy, M_i is the molecular weight of the species i, R is the gas constant, and T is the temperature. However, the Langmuir equation is accurate only at very low pressures, where significant condensation of the vapor does not take place. As a result, when welding is conducted at 1 atm, Eq. (14) predicts a much higher vaporization flux than the actual. The equilibrium vapor pressures of the various alloying elements over the respective pure liquids, necessary to calculate the vaporization flux, are presented in Table III.[48–51] Assuming that the alloy is ideal at high temperatures, the equilibrium vapor pressures of the various species over the alloy can be expressed as

$$P_i = X_i P_i^0, \tag{15}$$

where X_i is the mole fraction of the element i in the alloy and P_i^0 is the equilibrium vapor pressure of the element i over the pure liquid. The computed vapor pressures of alloying elements over the pure liquids and over 304 stainless steel at various temperatures are shown in Fig. 4. It can be seen from Fig. 4(a) that in the entire temperature range, the vapor pressure of manganese over its pure liquid is the highest. However, its vapor pressure over the alloy is lower than those of iron and chromium, as observed from Fig. 4(b). This behavior is consistent with the fact that manganese only accounts for 1.0 wt% in 304 stainless steel whereas iron and chromium are present at 72.3 and 18.1 wt%, respectively.

Figure 5 shows that computed temperature distribution and total vapor fluxes on the weld pool surface after 3.0 ms calculated by the model and the Langmuir equation. Because the vapor pressure of all the alloying elements are strong functions of temperature (as shown in Fig. 4), both distribution patterns of the vapor fluxes are similar to the surface temperature profiles. From Fig. 5(a), the peak temperature near the weld center of the beam-workpiece interaction zone exceeds the boiling point of the alloy. As a result, the vaporization here is predominantly driven by the pressure gradient. Most of the vaporization from the weld pool surface occurs from this active region. The diameter of this region is approximately 0.2 mm, as can be observed from Fig. 5(b). This dimension is comparable but somewhat smaller than the

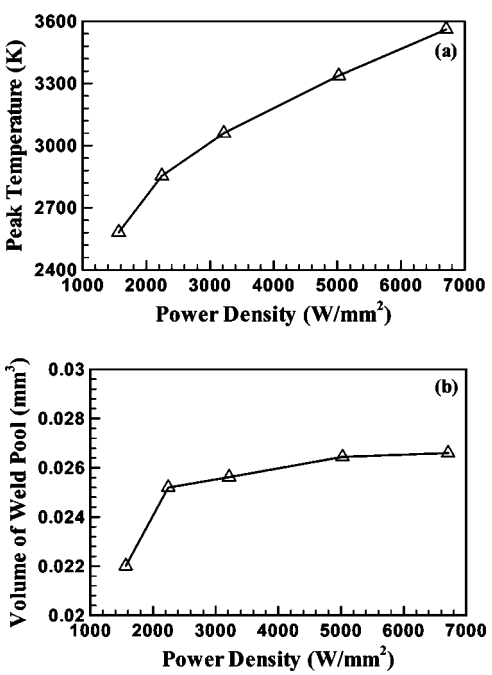

FIG. 3. Effects of laser power density on (a) the computed peak temperature pulse and (b) the computed volume of the weld pool. Laser power: 1067 W, and duration: 3 ms.

TABLE III. Vapor pressure of different elements as a function of temperature.

Elements	The equilibrium vapor pressures[a] over pure liquid (atm)
Fe	$\log(P^0\times 760) = 11.5549 - 1.9538\times 10^4/\mathrm{T} - 0.62549\ \log \mathrm{T} - 2.7182\times 10^{-9}\ \mathrm{T} + 1.9086\times 10^{-13}\ \mathrm{T}^2$
Mn	$\log(P^0\times 1.013\times 10^5) = -5.58\times 10^{-4}\ \mathrm{T} - 1.503\times 10^{-4}/\mathrm{T} + 12.609$
Cr	$\log(P^0\times 1.013\times 10^5) = -13.505\times 10^3/\mathrm{T} + 33.658\ \log \mathrm{T} - 9.29\times 10^{-3}\ \mathrm{T} + 8.381\times 10^{-7}\ \mathrm{T}^2 - 87.077$
Ni	$\log P^0 = 6.666 - 20765/\mathrm{T}$

[a]See Reference. 48–51.

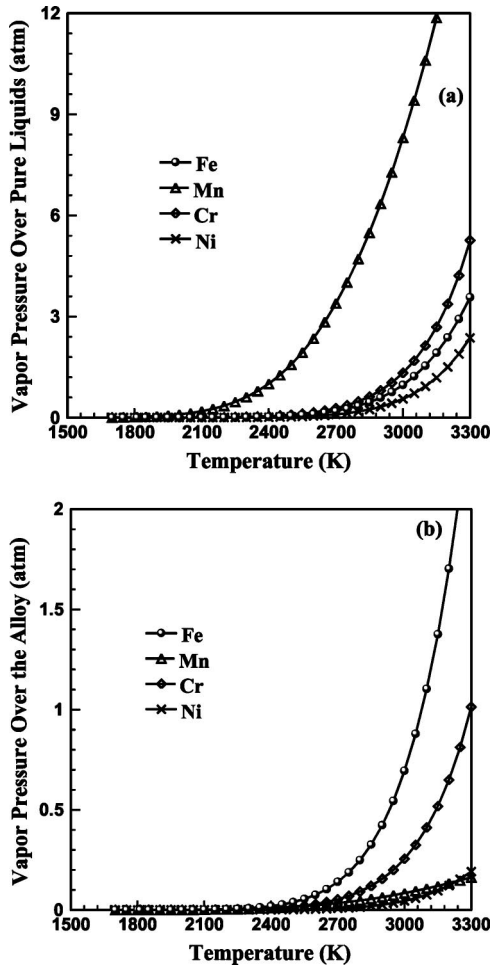

FIG. 4. Equilibrium vapor pressures of the various alloying elements (a) over respective pure liquids and (b) over 304 stainless steel as a function of temperature.

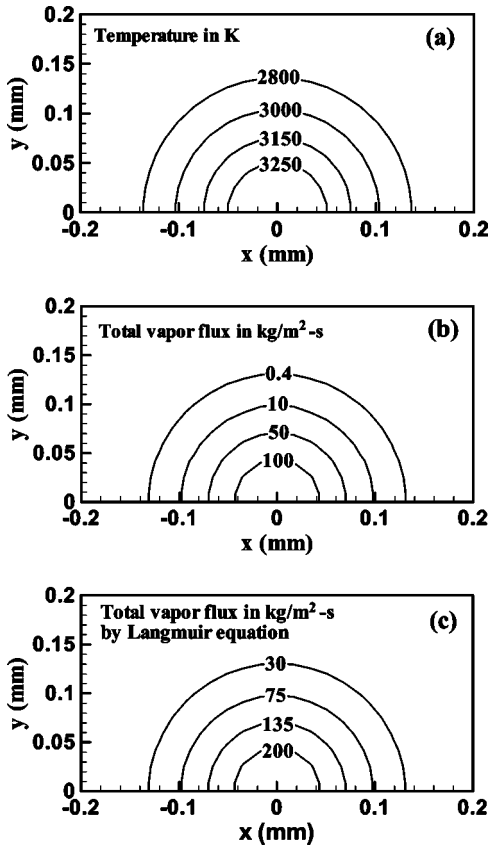

FIG. 5. Distribution of temperature and the total vapor flux on the weld pool surface after 3 ms. Laser power: 1067 W, pulse duration: 3 ms, and beam radius: 0.26 mm.

laser-beam diameter of 0.52 mm. The vaporization flux outside this region is much lower because it is driven mainly by the concentration gradient. Figure 5 also shows that the vapor flux calculated by the Langmuir equation in 5(c) is higher than that computed by the model in 5(b). At higher temperatures, the vapor flux calculated by the Langmuir equation is twice as much as that computed by the model. At lower temperatures, the difference is much more significant. The vapor flux calculated by the Langmuir equation is 7–75 times as much as that computed by the model.

Figure 6 shows the variation of the vaporization rates with time as calculated by the model and the Langmuir equation. It can be seen that the vaporization rates of the constituent alloying elements increase with time. At the end of pulse cycle, vaporization rates decrease suddenly and the vaporization of the alloying elements stops. The time-dependent vaporization rate is determined by the changes in the temperature distribution at the surface of the weld pool as shown in Figs. 1 and 2(a). From Fig. 6, it can be also seen that iron is the main vaporizing species, followed by chromium and manganese. Although manganese has the highest vapor pressure over its pure liquid, its low equilibrium vapor pressure over the alloy results in a lower vaporization rate than either iron or chromium.

C. Composition change

Figure 7 shows the typical concentration profiles of Fe, Cr, Ni, and Mn after laser spot welding of 304 stainless steel determined by the electron microprobe analysis. It is observed that the concentrations of the constituent elements in the fusion zone are different from those in the base metal. The concentrations of manganese and chromium in the weld pool are lower than those in the base metal because of vaporization. In contrast, the concentrations of iron and nickel in the fusion zone are higher than those in the base metal, and these results need some discussion. Although the total mass of iron and nickel in the weld pool is lower than those before the welding, the total mass of the weld pool has decreased at a higher proportion because of the loss of manganese, chromium, iron, and nickel. As a result, the concentrations of iron and nickel in the fusion zone are higher than those in the base metal because of the loss of manganese and chromium. Although this behavior may appear counterintuitive, it is consistent with Eq. (12).

The computed changes in the concentrations of the constituent alloying elements, as a function of time, are shown in Fig. 8(a). In the first millisecond, the concentration change of the alloying elements is small due to the low temperature. After that, the vaporization rate increases due to increase in temperature, and as a result, the concentrations of alloying elements significantly increase with time. It can be seen that the concentrations of manganese and chromium decrease, whereas those of iron and nickel increase due to the laser

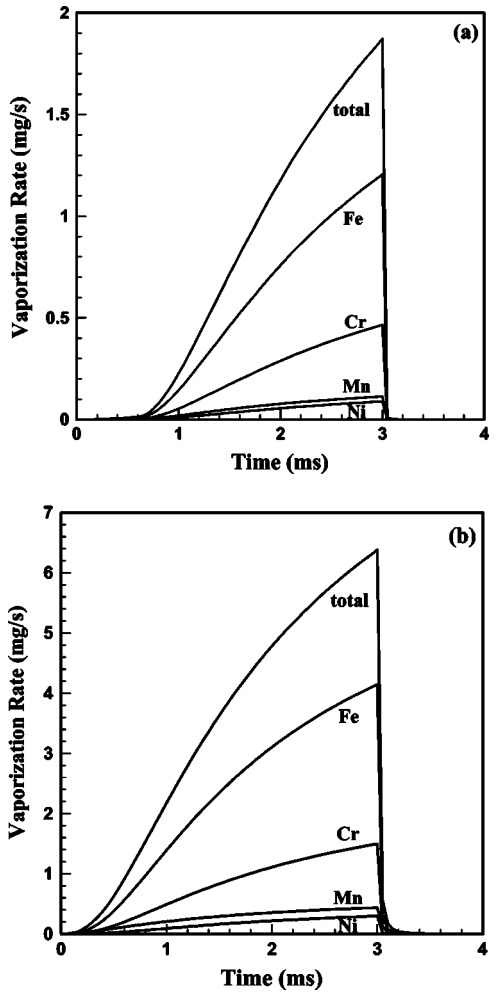

FIG. 6. Change of vaporization rates of the four alloying elements with time calculated by (a) the model and (b) the Langmuir equation. Laser power: 1067 W, pulse duration: 3 ms, and beam radius: 0.26 mm.

spot welding. This behavior is similar to the experimental results presented in Fig. 7. Figure 8(b) shows that the change in the concentration becomes more pronounced with the increase in the laser power density, resulting from higher temperatures. At the highest laser power density, the absolute values of the concentration changes of iron and chromium are 0.327 and 0.375 wt%, respectively, which are higher than the composition changes of nickel and manganese. This is mainly due to the high concentrations of iron and chromium in the weld metal.

The comparison between the experimental and computed concentration changes of the various alloying elements is shown in Fig. 9. The fair agreement between the experimental and the computed concentration changes of manganese, as a function of power density, can be seen in Fig. 10. In experiments, several electron microprobe traces were made for each sample. From Eq. (12), the final concentration is affected by two factors: the volume of the weld pool and the total weight loss. As the laser power density increases, both the volume and the total weight loss increase. As a result, the change of concentration with laser power density is not monotonic. Depending on how the rates of total weight loss and volume change with power density, the value of the con-

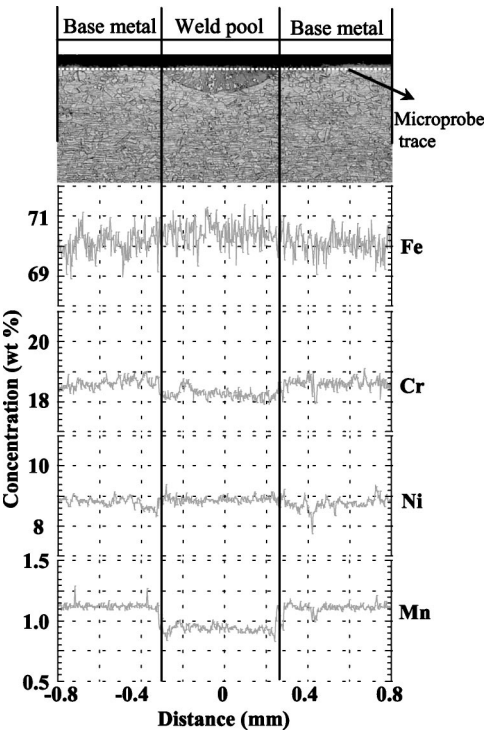

FIG. 7. Concentration profiles of the various alloying elements traced by electron microprobe after the laser spot welding. Laser power: 1067 W, pulse duration 3 ms, and beam radius: 0.325 mm.

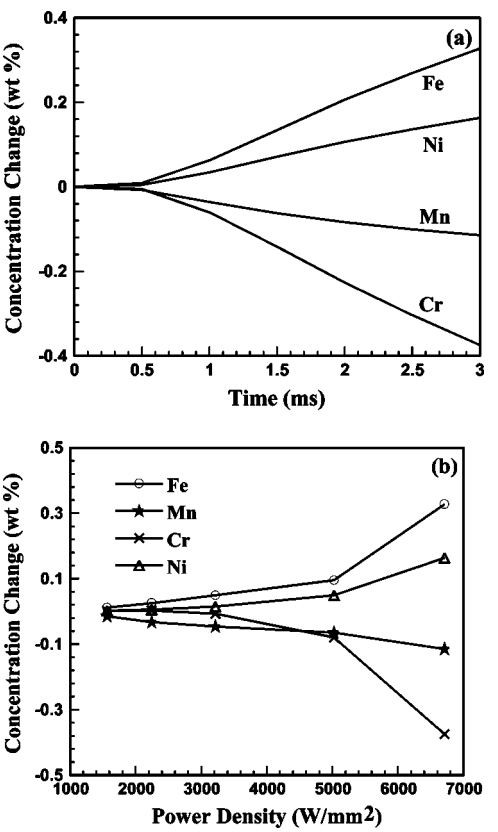

FIG. 8. (a) Concentration change of the various alloying elements as a function of time. Laser power: 1067 W, pulse duration 3 ms, and beam radius: 0.225 mm; (b) Concentration change of the various alloying elements as a function of power density. Laser power: 1067 W and pulse duration: 3 ms.

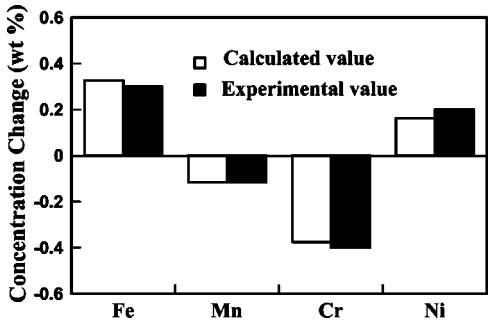

FIG. 9. Comparison between the calculated and the experimentally determined composition change of 304 stainless steel. Laser power: 1067 W, pulse duration: 3 ms, and beam radius: 0.225 mm.

centration change either increases or decreases. Because the concentration change of the alloying elements has effects on the mechanical or corrosion properties of the alloys, the successful prediction of the composition change by the model is helpful to understand how these properties are affected by laser spot welding.

V. SUMMARY AND CONCLUSIONS

A comprehensive model to calculate the temperature, the vaporization rates of the alloying elements, and the weld metal composition change during laser microjoining with 200 μm deep spot welds of 304 stainless steel, taking into account both the vaporization and condensation, was developed. During laser spot welding, the peak temperatures and the volume of the weld pool increased with time and laser power density. At high power densities, the computed temperatures on the weld pool surface were found to be higher than the boiling point of 304 stainless steel. As a result, vaporization of the alloying elements resulted from both the pressure and the concentration gradients. The vaporization rates and concentration changes of the constituent alloying elements were predicted by the model. The calculations show that the concentrations of manganese and chromium decreased, whereas the concentrations of iron and nickel increased owing to welding. The composition change predicted by the model was in fair agreement with the corresponding experimental results for spot welds of a few millisecond duration and a few hundred micrometer depth.

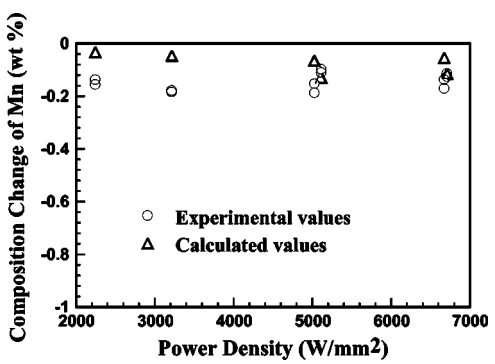

FIG. 10. Experimental and calculated concentration change of manganese as a function of power density. Pulse duration: 3 ms.

ACKNOWLEDGMENTS

This work was supported by a grant from the U.S. Department of Energy, Office of Basic Energy Sciences, Division of Materials Sciences, under Grant No. DE-FGO2-01ER45900. Portions of this work, performed at Sandia National Laboratories, were supported by the United States Department of Energy's National Nuclear Security Administration under Contract No. DE-AC04-94AL85000. The authors would like to thank J. Norris and P. Hlava for their help with the experimental measurements and S. Mishra for his interest in the work.

[1]X. He, P. W. Fuerschbach, and T. DebRoy, J. Phys. D **36**, 1388 (2003).
[2]A. Block-Bloten and T. W. Eagar, Metall. Trans. B **15**, 461 (1984).
[3]G. J. Dunn, C. D. Allemand, and T. W. Eagar, Metall. Trans. A **17**, 1851 (1986).
[4]G. J. Dunn and T. W. Eager, Metall. Trans. A **17**, 1865 (1986).
[5]A. Blake and J. Mazumder, J. Eng. Ind. **107**, 275 (1985).
[6]D. W. Moon and E. A. Metzbower, Weld. J. (Miami, FL, U. S.) **62**, 53s (1983).
[7]M. J. Cieslak and P. W. Fuerschbach, Metall. Trans. B **19**, 319 (1988).
[8]K. Mundra and T. DebRoy, Metall. Trans. B **24**, 145 (1993).
[9]H. Zhao and T. DebRoy, Metall. Mater. Trans. B **32**, 163 (2001).
[10]P. A. A. Khan and T. Debroy, Metall. Trans. B **15**, 641 (1984).
[11]M. M. Collur, A. Paul, and T. DebRoy, Metall. Trans. B **18**, 733 (1987).
[12]X. He, T. DebRoy, and P. W. Furerschbach, J. Appl. Phys. **94**, 6949 (2003).
[13]S. A. Dravid and T. DebRoy, Science **257**, 497 (1992).
[14]T. DebRoy and S. A. Dravid, Rev. Mod. Phys. **67**, 85 (1995).
[15]H. Zhao, D. R. White, and T. DebRoy, Int. Mater. Rev. **44**, 238 (1999).
[16]G. M. Oreper, J. Szekely, and T. W. Eager. Metall. Trans. B **17**, 735 (1986).
[17]S. Kou and D. K. Sun, Metall. Trans. A **16**, 203 (1985).
[18]S. Kou and Y. H. Wang, Metall. Trans. A **17**, 2271 (1986).
[19]M. C. Tsai and S. Kou, Int. J. Numer. Methods Fluids **9**, 1503 (1989).
[20]S. Kou and Y. H. Wang, Weld. J. (Miami, FL, U. S.) **65**, 63s (1986).
[21]C. Chan, J. Mazumder, and M. M. Chen, Metall. Trans. A **15**, 2175 (1984).
[22]K. Mundra, T. DebRoy, and K. M. Kelkar, Numer. Heat Transfer, Part A **29**, 115 (1996).
[23]W. Pitscheneder, T. DebRoy, K. Mundra, and R. Ebner, Weld. J. (Miami, FL, U. S.) **75**, 71s (1996).
[24]A. Paul and T. DebRoy, Metall. Trans. B **19**, 851 (1988).
[25]Z. Yang and T. DebRoy, Sci. Technol. Weld. Joining **2**, 53 (1997).
[26]Z. Yang and T. DebRoy, Metall. Mater. Trans. B **30**, 483 (1999).
[27]W. Zhang, J. W. Elmer, and T. DebRoy, Mater. Sci. Eng., A **333**, 320 (2002).
[28]T. Hong, W. Pitscheneder, and T. DebRoy, Sci. Technol. Weld. Joining **3**, 33 (1998).
[29]T. Hong and T. DebRoy, Metall. Mater. Trans. B **34**, 267 (2003).
[30]T. Hong and T. DebRoy, Ironmaking Steelmaking **28**, 450 (2001).
[31]S. Sista and T. DebRoy, Metall. Mater. Trans. B **32**, 1195 (2001).
[32]Z. Yang, S. Sista, J. W. Elmer, and T. DebRoy, Acta Mater. **48**, 4813 (2000).
[33]S. Sista, Z. Yang, and T. DebRoy, Metall. Mater. Trans. B **31**, 529 (2000).
[34]H. Zhao and T. DebRoy, J. Appl. Phys. **35**, 10089 (2003).
[35]W. Zhang, G. Roy, J. Elmer, and T. DebRoy, J. Appl. Phys. **93**, 3022 (2003).
[36]X. He, T. DebRoy, and P. W. Fuerschbach, J. Phys. D **36**, 3079 (2003).
[37]P. Sahoo, M. M. Collur, and T. Debroy, Metall. Trans. B **19**, 967 (1988).
[38]D. Peckner and I. M. Bernstein, *Handbook of Stainless Steels* (McGraw-Hill Book Company, New York, 1977).
[39]P. W. Fuerschbach and J. T. Norris, presented at the ICALEO 2002 on Beam Characterization for Nd:YAG Spot Welding Lasers, Scottsdale, AZ, 2002.
[40]J. R. Davis, *Metals Handbook* (ASM International, Materials Park, OH, 1998).
[41]*ASM Specialty Handbook* (ASM International, Materials Park, OH, 1994).
[42]Metals Handbook (ASM international, Materials Park ,OH, 1990), Vol. 1.
[43]E. U. Schlunder and V. Gniclinski, Chem.-Ing.-Tech. **39**, 578 (1967).
[44]S. I. Anisimov and A. Kh Rakhmatulina, Sov. Phys. JETP **37**, 441 (1973).

[45]C. J. Knight, AIAA J. **17**, 519 (1979).
[46]W. G. Vincenti and C. H. Kruger, *Introduction to Physical Gas Dynamics* (Wiley, New York, 1965).
[47]S. Dushman, *Scientific Foundations of Vacuum Technique* (Wiley, New York, 1962).
[48]R. Hultgren, P. D. Desai, D. T. Hawkins, M. Gleiser, K. K. Kelley, and D. D. Wagman, *Selected Values of the Thermodynamic Properties of the Elements* (ASM International, Materials Park, OH, 1973).
[49]R. E. Honig and D. A. Kramer, *Physicochemical Measurements in Metal Research* (Interscience Publishers, New York, 1970).
[50]C. L. Yaws, *Handbook of vapor pressure* (Gulf Pub. Co., Houston, 1994).
[51]C. B. Alcock, V. P. Itkin, and M. K. Horrigan, Can. Metall. Q. **23**, 309 (1984).